Int. J. Electrochem. Sci., 14 **(2019)** 4034 – 4046, doi: 10.20964/2019.05.42

International Journal of
ELECTROCHEMICAL
SCIENCE
www.electrochemsci.org

High Performance of Chitosan Derived Porous Carbon as Supercapacitor Electrodes

Mengying Yuan[1], *Lihua Liu*[2], *Ben Niu*[1], *Feng Jiang*[1], *Mei Li*[1,3,4,*]

[1] School of Materials Science and Engineering, Qilu University of Technology (Shandong Academy of Sciences), Jinan 250353, P.R. China.
[2] College of Resources and Environment, Linyi University, Linyi 276005, China.
[3] Shandong Provincial Key Laboratory of Processing and Testing Technology of Glass and Functional Ceramics, Jinan 250353, P.R. China.
[4] Key Laboratory of Amorphous and Polycrystalline Materials, Qilu University of Technology (Shandong Academy of Sciences), Jinan 250353, P.R. China.
[*]E-mail: lim@qlu.edu.cn

Received: 9 January 2019 / *Accepted:* 23 February 2019 / *Published:* 10 April 2019

Chitosan, a renewable biomass derivative, was used as electrode material with a facile pyrolysis and activation process for supercapacitors. The physical and electrochemical performances of the as-prepared chitosan-based hierarchical porous carbon (CHPC) were evidently affected by the mass ratio of powder to KOH and the carbonization temperature. The sample obtained at the best powder/KOH ratio of 1:1 exhibits meaningful structural characteristics: optimized interconnected hierarchical pore structure and high specific surface area (863.58 m^2 g^{-1}). It possesses excellent capacitive property with high specific capacitance of 310 F g^{-1} in 6 mol L^{-1} KOH electrolyte at a current density of 1 A g^{-1}, and enhanced rate capability (231 F g^{-1} can be retained at 10 A g^{-1}). Additionally, it shows excellent capacity retention of 80% after 10 000 cycles at 10 A g^{-1}. The efficiently combined and optimized synthesis process and the excellent electrochemical characteristics are of strategic guiding significance to the large-scale application of high-performance supercapacitors.

Keywords: High-performance; Chitosan; Hierarchical pores; Pyrolysis; KOH activation

1. INTRODUCTION

Supercapacitor is a new-generation energy storage device with excellent cycling stability, high power density and fast charge-discharge rate [1-4]. In order to improve the capability of energy storage and overcome the application limitations caused by low energy density, researchers have devoted many efforts in designing and developing electrode materials with excellent properties [5]. Different nanostructured carbon materials, such as graphene[6, 7], carbon nanotubes[8-10], activated carbons[11], carbon fibers[12] and porous carbons[13], have been widely developed and applied to fabricate

supercapacitors as electrode materials, primarily due to the high conductivity, physicochemistry stability and low cost. Recently, the porous carbon materials have shown broad application prospects in supercapacitors, owning to their large specific surface area, abundant porous structures and porosity [14-16].

Furthermore, the pores with different pore sizes, such as micropores (<2 nm), mesopores (2~50 nm) and macropores (>50 nm), have a remarkable impact on the electrochemical performance [17]. Micropores, prepared by activation process which is a simple and efficient method, can dramatically increase the specific surface areas and provide more active sites [18]. However, the micropores, located on the surface of carbon material, limit rapid transportation of electrolyte ions and rate discharge capability [19]. In contrast, mesopores can accelerate the diffusion of electrolyte ions which improves rate capacity; and macropores can be used as buffer memories for ionic electrolyte which can shorten the distance of ion diffusion [18, 20, 21]. Therefore, the electrode materials with interconnected hierarchical porous structures, which combine the advantages of micropores, mesopores and macropores, exhibit excellent electrochemical performances and show great potential in supercapacitors. The template methods (hard and soft templates) can also optimize the pore structure by controlling the size of template, while they are not suitable for large scale applications due to the tedious preparation process, low porosity and high cost [22-24]. Therefore, it is essential to find a suitable and simple method for preparing electrode materials with interconnected hierarchical porous structures.

Due to the consideration of the increased pressures on fossil fuels and environmental issues, biomass-based carbon materials, as the renewable and clean carbon sources, have been recognized in the recent years [25-31]. As we all know, chitosan is a straight-chain polymer with abundant amino-group (-NH_2) and hydroxyl-group (-OH), and it obtained from chitin by deacetylation reaction and widely existed in the nature [32]. The amino- and hydroxyl-groups successfully introduced the heteroatoms (nitrogen and oxygen) into carbon framework, which not only provide pseudo-capacitance, but also improve the wettability between electrode materials and electrolyte [33]. And the pseudo-capacitance is beneficial to the improvement of specific capacitance and rate capability of carbon materials [34-37]. Hence, chitosan, a promising carbon material with good performances used for electrode, has been extensively studied in recently years. The three-dimensional porous carbon foam (PCF) showed a high energy-storage capacity of 246.5 F g^{-1} at 0.5 A g^{-1} in 3 mol L^{-1} KOH and an ultra-high power density of 25 kW kg^{-1} at an energy density of 2.8 W h kg^{-1} [38]. The N-doped graphene-based hierarchical porous carbon aerogel exhibited a specific capacitance of 197 F g^{-1} at 0.2 A g^{-1} and displayed excellent cycling stability with a capacitance retention of about 92.1% over 10000 cycles [39]. Zhu et al. recently reported that chitosan-derived carbonaceous materials was synthesized from hydrothermal treatment and KOH activation, which displayed high specific capacitance of 305 F g^{-1} at the discharge/charge current density of 0.5 A g^{-1} and the energy density of 8.5 Wh kg^{-1} at a power density of 1 kW kg^{-1} in 6 M KOH aqueous solution [40].

In this work, chitosan-based hierarchical porous carbon (CHPC) was successfully synthesized *via* a simplified and efficient method combining pyrolysis with KOH activation. The key of the method is most functional groups and organic structure decompose at 300 ^oC, which is beneficial for further activation of KOH and the production of interconnected hierarchical porous structure. The as-prepared CHPC exhibits high specific surface area of 863.58 m^2 g^{-1} and the special interconnected pore structures

with different diameters. More specifically, the as-prepared samples exhibit high energy-storage capacity of 310 F g^{-1} at 1 A g^{-1}, and better cycle stability with 80% retention after 10 000 cycles at 10 A g^{-1}, and shows an energy density of 25 W h Kg^{-1} at a power density of 900 W kg^{-1} in 6 mol L^{-1} KOH electrolyte. Compared with other chitosan-based carbon materials shown above, the current research work has greatly improved both in terms of structural characteristics and energy storage performances.

2. EXPERIMENTAL

2.1. Materials

Chitosan (260,000 Daltons, average molecular weight) was purchased from Sinopharm Chemical Reagent Co., Ltd. Potassium hydroxide and hydrochloric acid (HCl) were both bought from Tianjin Baishi Chemical Industry Co., Ltd. All chemicals were analytical grade and without any treatment.

2.2. Preparation of CHPC

Typically, chitosan was pre-carbonized at 300 ^oC in Ar atmosphere with a heating rate of 2 ^oC min^{-1} and kept for 3 h. Then the obtained black powder was mixed with KOH at an appropriate weight ratio and ground in mortar. After drying, the mixture was calcined at different temperatures for 3 h with the same heating rate under Ar atmosphere. The as-prepared materials were soaked in 0.5 mol L^{-1} HCl solution, and washed with deionized water and ethanol in sequence until the neutral condition, followed by drying at 45 ^oC for 12h. As the mass ratio of powder/KOH and carbonization temperature are the crucial parameters in the activated process, CHPCs were prepared with different powder/KOH ratios (2:1, 1:1, 1:2) and activation temperatures (500, 600, 700, 800 ^oC). The chitosan-based hierarchical porous carbon materials (CHPC) were denoted as $CHPC_X$-Y, where X and Y represent the activated ratio and carbonization temperature, respectively. For comparing the effect of KOH, a control sample without KOH activation was prepared and denoted as CHPC-Y.

2.3. Characterization

The scanning electron microscope (SEM, Hitachi S4800) and transmission electron microscope (TEM, Tecnai G2 F20) were applied to analyze the morphology characteristics of the samples at an accelerated voltage of 20 KV and 200KV, respectively. The N_2 adsorption-desorption measurements were carried out by an Automated Gas Sorption Anlyzer (Autosorb-IQ) after vacuum degassing 12 h at 250~300 ^oC. The pore-size distribution and the pore parameters were analyzed by non-local density functional theory (NLDFT) and Brunauer-Emmett-Teller (BET), respectively. And the pore volume was derived from the amount of N_2 adsorbed in a relative pressure (P/P_0) about 0.99. The thermos-gravimetric analysis (TGA) was performed on Mettler Toledo Instrument from 45 ^oC to 800 ^oC under N_2 with a heating rate of 5 ^oC min^{-1}. The X-ray diffraction (XRD) patterns were measured by a D8-ADVANCE X-ray diffractometer (Cu Kα source, λ = 0.15406 Å) with the scan rate of 1^o min^{-1}. Raman spectra was performed on a Laser Confocal Micro-Raman Spectroscopy (LabRAM HR800) with an excitation wavelength of 532 nm and the argon ion laser source ranges from 600 cm^{-1} to 3600 cm^{-1}. The

X-ray photoelectron spectroscopy (XPS) was obtained from Multifunctional imaging electron spectrometer (Thermo ESCALAB 250XI) with the Al-Ka as the monochromatic source. The binding energy was referenced to the C 1s peak located at 284.8 eV.

2.4. Electrochemical measurements

The electrodes were prepared by mixing the samples, acetylene black and polyvinylidene fluoride (PVDF) at the weight ratio of 8:1:1 in the N-methyl-2-pyrrolidone into slurry, then the mixture was applied liberally to the stainless steel mesh and dried at 45 ^{o}C for 10 h (1 cm × 1 cm, about 2.5 mg). All the electrochemical performances were texted on a CHI660E electrochemical workstation using galvanostatic charge-discharge (GCD), cyclic voltammetry (CV), and electrical impedance spectroscopy (EIS) techniques in the 6 mol L^{-1} KOH electrolyte. The GCD and CV texts varied the constant current from 0.5 to 10 A g^{-1} and the scan rate from 10 to 100 mV s^{-1} within the voltage range of -0.1-1.1 V, respectively. The frequency range for the EIS was from 0.01 to 10^5 Hz with the open circuit potential.

In the typical three electrode system (half-cell), platinum plate and a standard mercuric oxide electrode were served as the counter electrode and reference electrode, respectively. The specific capacitance (C_{sp}, F g^{-1}) of the electrode can easily be deduced by GCD curves based on the equation (1) [41]:

$$C_{sp}=I\times\Delta t/\left(m_{sp}\times\Delta V\right) \quad (1)$$

In the symmetrical two electrode system (full-cell), two electrodes with same mass were back to back and separated by the polypropylene membrane. Similarly, the specific capacitance (C_{cell}, F g^{-1}) was also calculated according to equation (2) [42]:

$$C_{cell}=I\times\Delta t/(m_{cell}\times\Delta V) \quad (2)$$

The energy density (E_{cell}, W h Kg^{-1}) and power density (P_{cell}, W Kg^{-1}) were obtained through the equations (3) and (4) [43]:

$$E_{cell}=C_{cell}\times\Delta V^2/(2\times3.6) \quad (3)$$

$$P_{cell}=(E_{cell}\times3600)/\Delta t \quad (4)$$

Where I is the discharge current (A), Δt represents the discharge time (s), ΔV refers to the voltage window (V), and m_{sp} and m_{cell} (g) are the mass of active materials on a single electrode and the two electrodes, respectively.

3. RESULTS AND DISCUSSION

3.1. Material characterization

The morphologies and porous structure of the CHPC-600 and $CHPC_{11}$-600 were characterized by SEM and TEM photos. The SEM images (Fig. 1a and b) indicate that the CHPC-600 presents irregular bulk or particle structure with relatively smooth surface after carbonization. After the activation of KOH at the mass ratio of 1:1, the surface of $CHPC_{11}$-600 exhibits densely opened macro-/mesopores with a diameter ranged from several to hundreds of nanometers according to Fig. 1c and 1d. The disordered porous structure was obviously formed after the chemical activation with KOH.

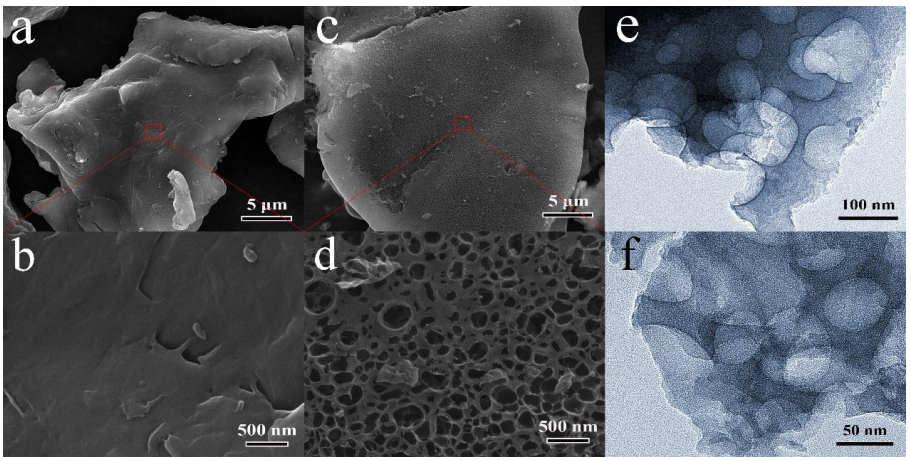

Figure 1. SEM images of CHPC-600 (a, b) and $CHPC_{11}$-600 (c, d), and TEM images of $CHPC_{11}$-600 (e, f) at different magnifications.

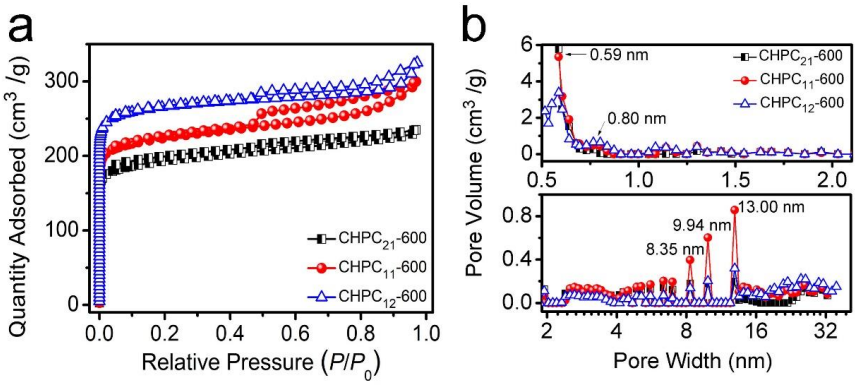

Figure 2. N_2 adsorption-desorption isotherms (a) and pore-size distributions (b) of the $CHPC_{21}$-600, $CHPC_{11}$-600 and $CHPC_{12}$-600 samples.

These hierarchical pores interconnected with each other and developed porous network structure, which are conducive to the transportation of the electrolyte and improve the electrochemical performances [44]. The porous structure of $CHPC_{11}$-600 can be observed more clearly in the TEM images. As is shown in Fig. 1e and f, the $CHPC_{11}$-600 is characteristic of void space structure, and the partial overlapped voids confirm the porous network structure which is consistent with the results of SEM (Fig. 1c and 1d). The interconnected porous structure largely shortens the ion transport distances and increases the diffusion speed of the electrolyte during the charge-discharge process, resulting in the improvement of rate performance [45].

Table 1. Pore parameters of the $CHPC_{21}$-600, $CHPC_{11}$-600 and $CHPC_{12}$-600 samples.

Samples	ratio	S_{BET} ($m^2\ g^{-1}$)	S_{micro} ($m^2\ g^{-1}$)	$S_{meso/macro}$ ($m^2\ g^{-1}$)	V_{pore} ($cm^3\ g^{-1}$)	V_{micro} ($cm^3\ g^{-1}$)	$V_{meso/macro}$ ($cm^3\ g^{-1}$)	D_{ave} nm
$CHPC_{21}$-600	2:1	752.81	612.19	140.62	0.35	0.24	0.11	1.87
$CHPC_{11}$-600	1:1	863.58	696.02	167.56	0.45	0.27	0.18	2.08
$CHPC_{12}$-600	1:2	1057.95	911.40	146.55	0.50	0.35	0.15	1.90

In order to explore how the dosage of KOH influences the porous characteristic and the pore parameters of obtained carbon materials, N_2 adsorption-desorption measurements were conducted. As shown in Fig. 2a, all of the three adsorption–desorption isotherms are similar in shape and have the typical characteristics of combination of type I and type IV [46]. What's more, the sharp rise in the adsorption capacity at the low relative pressure ($P/P_0 < 0.01$) and the obvious hysteresis loop at the high relative pressure ($P/P_0 > 0.4$), corresponding to the presence of abundant micropores and meso/macro-pores, respectively [47]. These results also confirm that the hierarchical porous structure does exist in carbon materials, caused by the pyrolysis and KOH activation. Additionally, it can be seen that the increasement of the dosage of KOH can dramatically impact the development of micropores and the adsorption capacity, and these also can be reflected by the pore parameters of the samples. As shown in Table 1, as the activated ratio increases to 1:1, the BET surface area, microporous and meso-/macroporous area increased markedly from 752.81 m^2 g^{-1}, 612.19 m^2 g^{-1} and 140.62 m^2 g^{-1} to 863.58 m^2 g^{-1}, 696.02 m^2 g^{-1} and 167.56 m^2 g^{-1}, respectively. These values show that KOH activation can produce abundant porous structure, especially microporous, and improve porosity of the samples [48]. Interestingly, as the activation ratio continues to increase to 1:2, $CHPC_{12}$-600 displays the largest BET surface area (1057.95 m^2 g^{-1}) and the microporous surface area (911.40 m^2 g^{-1}), while the surface area and volume of meso-/macropores are lower than $CHPC_{11}$-600. The excess KOH results in the collapse of meso-/macroporous structure and forms more micropores which dramatically increase the surface area [49]. As shown in Fig. 2b, the micropore size of $CHPC_{12}$-600 is mainly concentrated on 0.5-0.6 nm, which is lower than that of $CHPC_{11}$-600. It is well known that abundant micropores with smaller pore size can augment surface area, but also impede the rapid transportation of electrolyte ions [50]. Therefore, the appropriate activating ratio of KOH to CHPC is a crucial parameter to regulate the surface area and pore structures which further decide the energy storage performances of the prepared carbon materials.

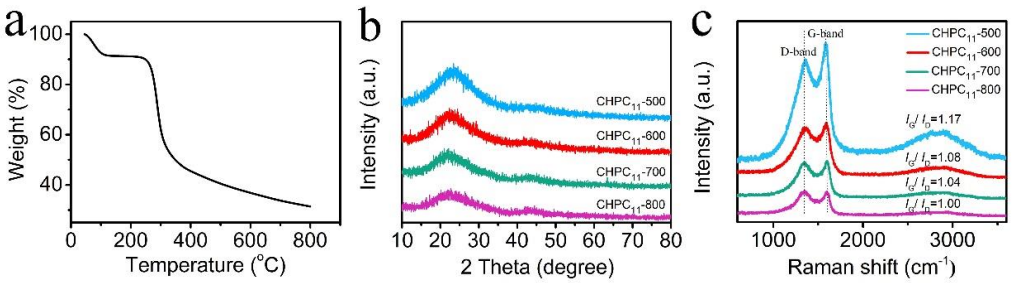

Figure 3. Thermal decomposition curve (a) of chitosan. XRD patterns (b) and Raman spectrum (c) of the $CHPC_{11}$-500, $CHPC_{11}$-600, $CHPC_{11}$-700 and $CHPC_{11}$-800.

The interconnected hierarchical porous structure and high specific area not only provide more spaces for energy storage, but also improve the transportation of electrolyte ions during the charge-discharge process, which have a positive effect on electrochemical performance and conductivity, especially the mass transfer resistance [51, 52].

Fig. 3a represents the TGA curve (around 45 °C-800 °C) of chitosan. And the curve shows a minor loss below 100 °C because of the evaporation of free water [53]. It is noteworthy that a sharp

weight loss at around 300 °C corresponds to the decomposition of functional groups and the organic structure of chitosan during pyrolysis [54]. Therefore, the pre-carbonation at 300 °C can produce some pores which are beneficial for the infiltration of KOH and the formation of interconnected hierarchical porous structure. And when the temperature reaches to 600 °C and 800 °C, the weight loss is around 64% and 69%, respectively, which show that chitosan has been carbonized. The XRD and Raman spectroscopies are usually employed to illustrate the crystal and graphitic structure of the samples. Fig. 3b and Fig. 3c give the XRD and Raman curves at four different carbonization temperatures. As shown in Fig. 3b, the obvious diffraction peaks at around 2θ=22°~24° can be observed, ascribing to the (002) crystal plane of graphitic carbon and suggesting the samples are graphitized which is beneficial for the increasement of electrical conductivity of carbon materials [55]. And the broad diffraction peaks confirm that as-prepared samples are amorphous carbons. Furthermore, the diffraction peak intensity at around 22°~24° was found to decrease gradually with the increasement of carbonization temperature from 500 °C to 800 °C, which suggests a decreased graphitization due to the decomposition of graphitic crystallites carbon atoms during activation process [56]. As displayed in the Fig. 3c, all the samples show two obvious characteristic peaks located at 1370 cm^{-1} (D-band) and 1594 cm^{-1} (G-band), which are related to the disorder and graphitic structure, respectively [57].

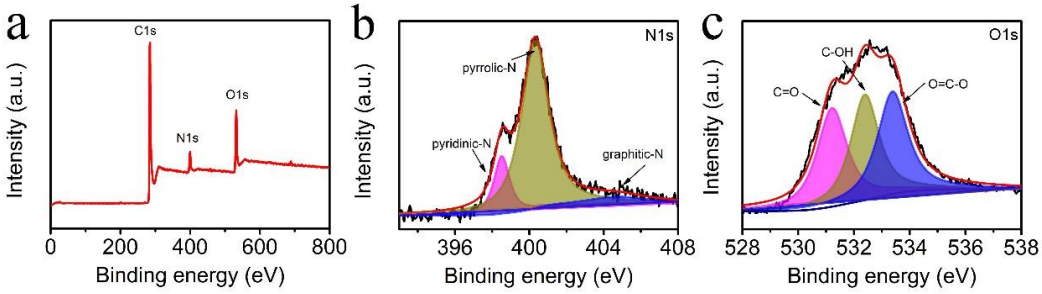

Figure 4. (a) XPS survey, (b) N1s, (c) O1s of $CHPC_{11}$-600.

The intensity ratios of G-band and D-band (I_G/I_D) usually demonstrate defective degree of the samples. As shown in Fig. 3c, the decreasing I_G/I_D ratio implies the generation of more defects though increasement of graphitization resulting from the higher carbonization temperatures [58]. The 2D band centered about 2859 cm^{-1} is the second order of the D band, which is sensitive to the number of graphene layers and indicates existence of multilayer graphene-like structure *[59, 60]*. And the decreased graphitization is in good agreement with the analysis of the XRD.

The surface elemental compositions and chemical bonding state of the $CHPC_{11}$-600 are further investigated by the XPS (Fig. 4). In the Fig. 4a, the three obvious speaks locate at 284.4, 400.7 and 531.4 eV, corresponding to C1s, N1s and O1s, respectively. The heteroatoms (nitrogen and oxygen) are beneficial for the promotion of electrochemical performance, because they not only provide the pseudo-capacitance but also improve the wettability between electrode material and electrolyte [61]. High-resolution XPS spectra are employed to analysis the electronic and atom binding states. The N1s is decomposed into three peaks located at 398.5, 400.3 and 404.8 eV, which associated with pyridinic-N, pyrrolic-N and graphitic-N, respectively [62]. In particular, the first two (pyridinic-N and pyrrolic-N) focus on improving the specific capacitance by introducing pseudocapacitance, while quaternary

graphitic-N can increase conductivity [63-65]. And the three peaks lie in 531.2, 532.4, and 533.4 eV of O1s spectra, corresponding to C=O, C-O, and O=C-O groups which contributes to the enhancement of wettability of materials [66, 67].

3.2. Electrochemical characterization

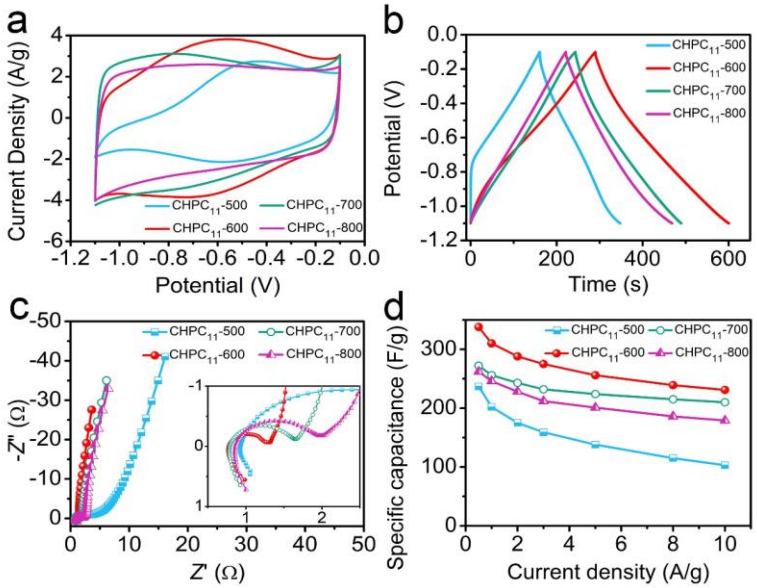

Figure 5. Electrochemical capacitive behaviors of the chitosan-based porous carbons at the activation temperature from 500 °C to 800 °C. (a) Cyclic voltammetry at a scan rate of 10 mV s^{-1}. (b) GCD curves at a current density of 1 A g^{-1}. (c) The Nyquist plots. (d) The dependence of capacitance as a function of current density.

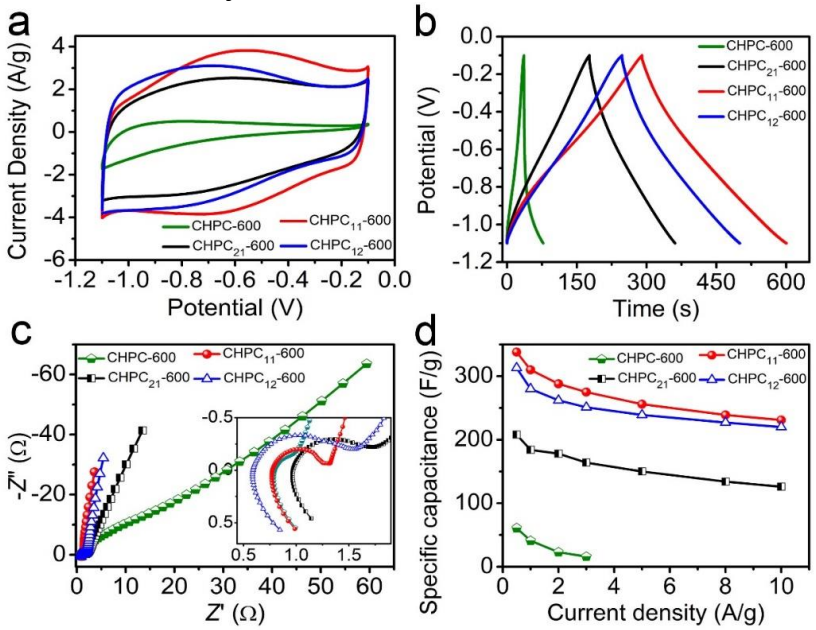

Figure 6. Electrochemical capacitive behaviors of the chitosan-based porous carbons at the different powder/KOH ratios (2:1, 1:1, 1:2). (a) Cyclic voltammetry at a scan rate of 10 mV s^{-1}. (b) GCD curves at a current density of 1 A g^{-1}. (c) The Nyquist plots. (d) The dependence of capacitance as a function of different current densities.

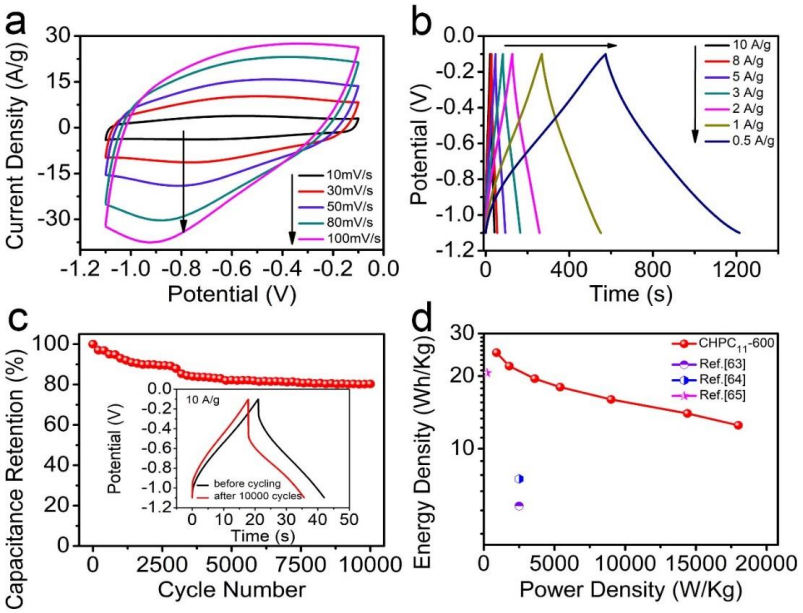

Figure 7. Electrochemical characterization of the $CHPC_{11}$-600 in 6 mol L^{-1} KOH aqueous electrolyte. (a) The CV curves at various scan rates. (b) GCD curves with different current densities. (c) Cyclic stability at a current density of 10 A g^{-1} over 10000 cycles. (d) The Ragone plot of $CHPC_{11}$-600.

The effects of activation temperature on electrochemical properties of the prepared porous carbon materials are shown in Fig. 5. The CV curve of $CHPC_{11}$-500 shows irregular and small square shape, and the low capacitance caused by poor carbonization are confirmed by the GCD curves in Fig. 5b. The CV curves show obvious redox peaks at 600 °C, mainly owing to the pseudo-capacitance resulted from nitrogen atom in the framework of CAC_{11}-600 [68]. With the increasing of activation temperature, the shape of the CV curves become more close to rectangle, suggesting that the electric double-layer capacitive behavior plays a more important role in the electric storage systems, while the effect of pseudo-capacitance has been minimized [69]. More obviously, the area bounded by the CV curve reaches the maximum at 600 °C, corresponding to the highest capacitance, which is demonstrated to the Fig. 5b and Fig. 5d. Accordingly, the specific capacitance of $CHPC_{11}$-600 is up to 310 F g^{-1} at 1 A g^{-1}, which is much higher than that of $CHPC_{11}$-500 (202 F g^{-1}), $CHPC_{11}$-700 (256 F g^{-1}) and $CHPC_{11}$-800 (246 F g^{-1}).

The specific capacitance values hint that the activation temperature is a significant condition to determine the electrochemical properties of the prepared carbon materials. The EIS test is also useful to evaluate the electrochemical properties of the chitosan-based porous carbon materials. From the Fig. 5c, a half semicircle and the intercept at the real axis in the high-frequency range and a line at low-frequency are shown, which represent the charge-transfer resistance (*R*ct), the solution resistance [70] and the ion-penetration diffusion process, respectively[69]. The $CHPC_{11}$-600 electrode has a semicircle with smallest diameter and a vertical curve, implying the fast charge transfer (lowest *R*ct) and ionic diffusion feature compared with others. So, the optimized activation temperature is 600 °C to get the best electrochemical properties. The analyses show that the higher activation temperature improves the conductivity of $CHPC_{11}$-600, but the too high temperature does reduce the effect of pseudo-capacitance

in electrochemical performance. Based on the points of high specific area, the optimized pore number and size, and the reasonable conductivity, the ideal activating carbonization temperature is 600 ºC.

Fig. 6 gives the electrochemical performances of the CHPC by changing the activation ratio of powder/KOH. The CV curves of the samples after KOH activation all deviate from the shape of a typical rectangle with obvious oxidation and deoxidization peaks, which is ascribed to the nitrogen atom existed in the carbon materials [42]. Furthermore, as the powder/KOH ratio increases, the $CHPC_{11}$-600 displays the optimal electrochemical performance (Fig. 6a and b), resulting from the appropriate specific surface and pore size as listed in Table 1. Although micropores can significantly increase specific surface area of $CHPC_{12}$-600, it decreases the average pore width and increases the diffusion resistance of electrolyte ion into samples. The Nyquist plots (Fig. 6c) determines the effects of KOH on diffusion and transfer resistance. Compared with other samples, the $CHPC_{11}$-600 curve has a semicircle with smallest diameter at high-frequency and a biggest slope at low-frequency, implying the fast charge transfer (lowest *R*ct) and ionic diffusion speed.

Table 2. Comparison of $CHPC_{11}$-600 with other biomass-derived carbon materials from recent references

Material name	Electrolyte	C_{sp} (F g^{-1})	Rate capability (F g^{-1})	Ref.
MAC-2	6 M KOH	310 (0.5 A g^{-1})	240 (5 A g^{-1})	[76]
CNFs-800	2 M H_2SO_4	140 (0.5 A g^{-1})	90 (20 A g^{-1})	[77]
Gelatin-Mg-Zn-1:5:3	6 M KOH	284.1 (1 A g^{-1})	88.7 (150 A g^{-1})	[78]
A-G/G-20	6 M KOH	252 (1 A g^{-1})	219 (10 A g^{-1})	[79]
LN600	1 M H_2SO_4	264 (1 A g^{-1})	-	[80]
A-NCs-800	6 M KOH	276 (1 A g^{-1})	192 (10 A g^{-1})	[81]
N-BBPCF	6 M KOH	210.6 (0.5 A g^{-1})	155 (2 A g^{-1})	[82]
$CHPC_{11}$-600	6 M KOH	310 (1 A g^{-1})	231 (10 A g^{-1})	This work

Rate capability of CHPC is the key to the application in energy materials and it is evaluated by GCD curves under various current densities according to the equation (1). As the current density increases from 1 A g^{-1} to 10 A g^{-1}, the capacitance of $CHPC_{11}$-600 gradually decreases from 310 F g^{-1} to 231 F g^{-1} and the retention rate reaches 75%, indicating the good rate property which can meet the demand of SCs under high current density. The long-term electrochemical stability of $CHPC_{11}$-600 is estimated by GCD curves at 10 A g^{-1} (Fig. 7c). After 10000 cycles, the capacity still remains 80%, demonstrating the excellent stability. A small reduction in capacitance is mainly due to the reduction of diffusion time for ions into the electrode surface [71]. To explore the energy and power density, the GCD curves of $CHPC_{11}$-600 was tested in two-electrode system using 6 mol L^{-1} KOH as electrolyte. The Ragone plot (Fig. 7c) shows that energy density is about 25 W h kg^{-1} (with the power density of 900 W Kg^{-1}) at 0.5 A g^{-1}, whereas it remains as high as 12.5 W h kg^{-1} (with the power density of 18000 W Kg^{-1}) at 10 A g^{-1} for $CHPC_{11}$-600, much superior to that of the other biomass-based electrode materials [72-74] and the commercial devices [75]. As shown in Tab. 2, the comparison of the as-prepared sample with other biomass-based carbon materials confirms that the $CHPC_{11}$-600 exhibits excellent specific capacitances and rate capability which can be used as a promising candidate for high performance electrode material.

4. CONCLUSIONS

In summary, chitosan-based hierarchical porous carbon materials were synthesized using bio-derived chitosan as carbon source *via* a simplified and efficient method combining pyrolysis with KOH activation. The mass ratio of power/KOH and the activation temperature play vital roles in enhancing the electrochemical performance. The appropriate mass ratios of power/KOH can increase the BET surface area (863.58 m^2 g^{-1}) and turns large lump materials into nanomaterials with hierarchical porous structure. Moreover, the appropriate activation temperature also contributes to the promotion of graphitization degree and pseudo-capacitance which can improve conductivity and charge storage capability. The $CHPC_{11}$-600 exhibit a high capacitance up to 310 F g^{-1} at 1 A g^{-1} and also is excellent in rate capability (231 F g^{-1} at 10 A g^{-1}) and cycling stability (remains 80%). The performances of the obtained carbon materials demonstrated that using renewable and environmentally friendly bio-derived carbon as precursor to produce electrode materials is a potential way for the application in energy storage systems.

ACKNOWLEDGMENTS
This work was supported by International Cooperation Foundation of Qilu University of Technology (QLUTGJHZ2018023) and International Intelligent Foundation of Qilu University of Technology (QLUTGJHZ2018024).

References

1. J. Yang, Y. Yuan, W. Wang, H. Tang, Z. Ye, J. Lu, *Journal of Power Sources*, 340 (2017) 6.
2. F. Béguin, V. Presser, A. Balducci, E. Frackowiak, *Advanced Materials*, 26 (2014) 2219.
3. Z.S. Wu, K. Parvez, X. Feng, K. Müllen, *Nature Communications*, 4 (2013) 2487.
4. J. Ding, H. Wang, Z. Li, K. Cui, D. Karpuzov, X. Tan, A. Kohandehghan, D. Mitlin, *Energy & Environmental Science*, 8 (2015) 941.
5. J. Wang, P. Nie, B. Ding, S. Dong, X. Hao, H. Dou, X. Zhang, *Journal of Materials Chemistry A*, 5 (2016) 2411.
6. A. Sarkar, A.K. Chakraborty, S. Bera, *Solar Energy Materials and Solar Cells*, 182 (2018) 314.
7. L. Mei, Y. Zhang, L. Yang, Y. Liu, J. Ma, *Journal of Materials Science Materials in Electronics*, 26 (2015) 485.
8. A. Sarkar, A.K. Chakraborty, S. Bera, S. Krishnamurthy, *The Journal of Physical Chemistry C*, 122 (2018) 18237.
9. I. Chakraborty, N. Chakrabarty, A. Senapati, A.K. Chakraborty, *The Journal of Physical Chemistry C*, 122 (2018) 27180.
10. N. Chakrabarty, A.K. Chakraborty, *Electrochimica Acta*, 297 (2019) 173.
11. M. Sevilla, R. Mokaya, *Energy & Environmental Science*, 7 (2014) 1250.
12. G. Zhang, Y. Song, H. Zhang, J. Xu, H. Duan, J. Liu, *Advanced Functional Materials*, 26 (2016) 2978.
13. T. Lin, I.W. Chen, F. Liu, C. Yang, H. Bi, F. Xu, F. Huang, *Science*, 350 (2015) 1508.
14. Y. Wang, Y. Liu, W. Liu, G. Zhang, G. Liu, H. Chen, JinlongYang, *Journal of Alloys & Compounds*, 677 (2016) 105.
15. L. Liu, Z. Niu, J. Chen, *Chemical Society Reviews*, 45 (2016) 4340.
16. M. Sevilla, R. Mokaya, *Energy & Environmental Science*, 7 (2014) 1250.
17. Z. Zhai, S. Wang, Y. Xu, L. Zhang, M. Yan, Z. Liu, *Journal of Solid State Electrochemistry*, 21 (2017) 1.
18. P. Cheng, S. Gao, P. Zang, X. Yang, Y. Bai, H. Xu, Z. Liu, Z. Lei, *Carbon*, 93 (2015) 315.

19. F. Su, C.K. Poh, J.S. Chen, G. Xu, D. Wang, Q. Li, J. Lin, X.W. Lou, *Energy & Environmental Science*, 4 (2011) 717.
20. L. Zhang, X. Yang, F. Zhang, G. Long, T. Zhang, K. Leng, Y. Zhang, Y. Huang, Y. Ma, M. Zhang, *Journal of the American Chemical Society*, 135 (2013) 5921.
21. M.C. Gutiérrez, F. Picó, F. Rubio, J.M. Amarilla, F.J. Palomares, M.L. Ferrer, F.D. Monte, J.M. Rojo, *Journal of Materials Chemistry*, 19 (2009) 1236.
22. D. Jiang, T.Y. Xiong, X. Fan, M.M. Li, C.L. Han, Y.T. Gong, H.Y. Wang, W. Yong, *Green Chemistry*, 17 (2015) 4053.
23. D.D. Zhou, H.J. Liu, Y.G. Wang, C.X. Wang, Y.Y. Xia, *Journal of Materials Chemistry*, 22 (2011) 1937.
24. Y. Zhai, Y. Dou, D. Zhao, P.F. Fulvio, R.T. Mayes, S. Dai, *Advanced Materials*, 23 (2011) 4828.
25. M. Genovese, K. Lian, *Journal of Materials Chemistry A*, 5 (2017)
26. J. Hou, K. Jiang, R. Wei, M. Tahir, X. Wu, M. Shen, X. Wang, C. Cao, *ACS Appl Mater Interfaces*, 9 (2017) 30626.
27. X.L. Wu, T. Wen, H.L. Guo, S. Yang, X. Wang, A.W. Xu, *Acs Nano*, 7 (2013) 3589.
28. Z.L. Wang, D. Xu, H.X. Zhong, J. Wang, F.L. Meng, X.B. Zhang, *Science Advances*, 1 (2015) e1400035.
29. Y. Hu, X. Tong, H. Zhuo, L. Zhong, X. Peng, *ACS Sustainable Chemistry & Engineering*, 5 (2017) 8663.
30. X. Zheng, J. Luo, W. Lv, D.W. Wang, Q.H. Yang, *Adv Mater*, 27 (2015) 5388.
31. Z. Xiao, W. Chen, K. Liu, P. Cui, D. Zhan, *International Journal of Electrochemical Science*, 13 (2018) 5370.
32. P.K. Dutta, S. Tripathi, G.K. Mehrotra, J. Dutta, *Food Chemistry*, 114 (2009) 1173.
33. L.F. Chen, X.D. Zhang, H.W. Liang, M. Kong, Q.F. Guan, P. Chen, Z.Y. Wu, S.H. Yu, *Acs Nano*, 6 (2012) 7092.
34. Y. Chen, X. Zhang, D. Zhang, P. Yu, Y. Ma, *Carbon*, 49 (2011) 573.
35. C. Long, D. Qi, T. Wei, J. Yan, L. Jiang, Z. Fan, *Advanced Functional Materials*, 24 (2014) 3953.
36. H.M. Jeong, J.W. Lee, W.H. Shin, Y.J. Choi, H.J. Shin, J.K. Kang, J.W. Choi, *Nano Letters*, 11 (2011) 2472.
37. F. Béguin, K. Szostak, G. Lota, E. Frackowiak, *Advanced Materials*, 17 (2005) 2380.
38. F. Zhang, T. Liu, G. Hou, T. Kou, L. Yue, R. Guan, Y. Li, *Nano Research*, 9 (2016) 2875.
39. P. Hao, Z. Zhao, Y. Leng, J. Tian, Y. Sang, R.I. Boughton, C.P. Wong, H. Liu, B. Yang, *Nano Energy*, 15 (2015) 9.
40. L. Zhu, F. Shen, R.L. Smith, X. Qi, *Energy Technology*, 5 (2017)
41. L. Xie, G. Sun, F. Su, X. Guo, Q. Kong, X. Li, X. Huang, L. Wan, W. song, K. Li, C. Lv, C.-M. Chen, *Journal of Materials Chemistry A*, 4 (2016) 1637.
42. B. Xu, S. Hou, G. Cao, F. Wu, Y. Yang, *Journal of Materials Chemistry*, 22 (2012) 19088.
43. H. Tang, J. Wang, H. Yin, H. Zhao, D. Wang, Z. Tang, *Adv Mater*, 27 (2015) 1117.
44. Z. Chen, K. Liu, S. Liu, L. Xia, J. Fu, X. Zhang, C. Zhang, B. Gao, *Electrochimica Acta*, 237 (2017) 102.
45. J. Wang, K.Y. Ma, J. Zhang, F. Liu, J. Cheng, *Journal of Colloid and Interface Science*, 507 (2017) 290.
46. K.S.W. Sing, *Pure and Applied Chemistry*, 57 (1985) 603.
47. M. Thommes, K. Kaneko, A.V. Neimark, J.P. Olivier, F. Rodriguez-Reinoso, J. Rouquerol, K.S.W. Sing, *Pure and Applied Chemistry*, 87 (2015)
48. F. Kurosaki, H. Koyanaka, M. Tsujimoto, Y. Imamura, *Carbon*, 46 (2008) 850.
49. C. Chang, X. Yang, S. Xiang, X. Lin, H. Que, M. Li, *Journal of the Electrochemical Society*, 164 (2017) A1601.
50. M.V. Navarro, N.A. Seaton, A.M. Mastral, R. Murillo, *Carbon*, 44 (2006) 2281.
51. K. Sun, S. Yu, Z. Hu, Z. Li, G. Lei, Q. Xiao, Y. Ding, *Electrochimica Acta*, 231 (2017) 417.

52. D. Wang, S. Liu, L. Jiao, G. Fang, G. Geng, J. Ma, *Carbon*, 119 (2017) 30.
53. G. Chen, C. Qiao, Y. Wang, J. Yao, *Australian Journal of Chemistry*, 67 (2014) 1532.
54. C. Qiao, X. Ma, J. Zhang, J. Yao, *Food Chemistry*, 235 (2017) 45.
55. Y. Cai, Y. Luo, Y. Xiao, X. Zhao, Y. Liang, H. Hu, H. Dong, L. Sun, Y. Liu, M. Zheng, *ACS Appl Mater Interfaces*, 8 (2016) 33060.
56. Z.J. Zhang, P. Cui, X.Y. Chen, J.W. Liu, *Journal of Solid State Electrochemistry*, 17 (2013) 1749.
57. Y. Wang, D.C. Alsmeyer, R.L. McCreery, *Chemistry of Materials*, 2 (1990) 557.
58. J. Hou, K. Jiang, M. Tahir, X. Wu, F. Idrees, M. Shen, C. Cao, *Journal of Power Sources*, 371 (2017) 148.
59. J. Luo, W. Zhong, Y. Zou, C. Xiong, W. Yang, *ACS Appl Mater Interfaces*, 9 (2017) 317.
60. L. Mei, Y. Zhang, L. Yang, Y. Liu, J. Yao, *Journal of Electrochimica Acta*, 166 (2015) 310.
61. Y. Zhang, X. Liu, S. Wang, S. Dou, L. Li, *Journal of Materials Chemistry A*, 4 (2016) 10869.
62. L.B. Xing, J.L. Zhang, J. Zhang, S.F. Hou, J. Zhou, W. Si, H. Cui, S. Zhuo, *Electrochimica Acta*, 176 (2015) 1288.
63. M. Seredych, D. Hulicova-Jurcakova, Q.L. Gao, T.J. Bandosz, *Carbon*, 46 (2008) 1475.
64. L.B. Xing, S.F. Hou, J.L. Zhang, J. Zhou, Z. Li, W. Si, S. Zhuo, *Materials Letters*, 147 (2015) 97.
65. P. Chen, J.J. Yang, S.S. Li, Z. Wang, T.Y. Xiao, Y.H. Qian, S.H. Yu, *Nano Energy*, 2 (2013) 249.
66. D. Hulicova-Jurcakova, M. Seredych, Q.L. Gao, T.J. Bandosz, *Advanced Functional Materials*, 19 (2010) 438.
67. L. Hao, X. Li, L. Zhi, *Advanced Materials*, 25 (2013) 3899.
68. L. Hao, B. Luo, X. Li, M. Jin, Y. Fang, Z. Tang, Y. Jia, M. Liang, A. Thomas, J. Yang, L. Zhi, *Energy & Environmental Science*, 5 (2012) 9747.
69. J. Cai, H. Niu, H. Wang, H. Shao, J. Fang, J. He, H. Xiong, C. Ma, T. Lin, *Journal of Power Sources*, 324 (2016) 302.
70. A. Bello, N. Manyala, F. Barzegar, A.A. Khaleed, D.Y. Momodu, J.K. Dangbegnon, *Rsc Advances*, 6 (2016) 1800.
71. D.S. Dhawale, G.P. Mane, S. Joseph, C. Anand, K. Ariga, A. Vinu, *Chemphyschem*, 14 (2013) 1563.
72. Y. Ba, W. Pan, S. Pi, Y. Zhao, L. Mi, *Rsc Advances*, 8 (2018) 7072.
73. B. Li, Y. Cheng, L. Dong, Y. Wang, J. Chen, C. Huang, D. Wei, Y. Feng, D. Jia, Y. Zhou, *Carbon*, 122 (2017) 592.
74. J. Huang, Y. Liang, H. Hu, S. Liu, Y. Cai, H. Dong, M. Zheng, Y. Xiao, Y. Liu, *Journal of Materials Chemistry A*, 5 (2017) 24775.
75. A. Burke, *Electrochimica Acta*, 53 (2008) 1083.
76. Y.T. Li, Y.T. Pi, L.M. Lu, S.H. Xu, T.Z. Ren, *Journal of Power Sources*, 299 (2015) 519.
77. S.-C. Li, B.-C. Hu, Y.-W. Ding, H.-W. Liang, C. Li, Z.-Y. Yu, Z.-Y. Wu, W.-S. Chen, S.-H. Yu, *Angewandte Chemie International Edition*, 57 (2018) 7085.
78. X.Y. Chen, C. Chen, Z.J. Zhang, D.H. Xie, *Journal of Materials Chemistry A*, 1 (2013)
79. H. Fan, W. Shen, *ACS Sustainable Chemistry & Engineering*, 4 (2015) 1328.
80. E. Raymundo-Piñero, M. Cadek, F. Béguin, *Advanced Functional Materials*, 19 (2009) 1032.
81. H. Wei, H. Chen, N. Fu, J. Chen, G. Lan, W. Qian, Y. Liu, H. Lin, S. Han, *Electrochimica Acta*, 231 (2017) 403.
82. B. Liu, L. Zhang, P. Qi, M. Zhu, G. Wang, Y. Ma, X. Guo, H. Chen, B. Zhang, Z. Zhao, B. Dai, F. Yu, *Nanomaterials (Basel)*, 6 (2016)